

# Registration of MR prostate images with biomechanical modeling and nonlinear parameter estimation

Ron Alterovitz<sup>a)</sup>

Department of Industrial Engineering and Operations Research, University of California, Berkeley,  
4141 Etcheverry Hall, Berkeley, California 94720-1777

Ken Goldberg

Department of Industrial Engineering and Operations Research and Department of Electrical Engineering  
and Computer Science, University of California, Berkeley, 4141 Etcheverry Hall,  
Berkeley, California 94720-1777

Jean Pouliot, I-Chow Joe Hsu, and Yongbok Kim

Department of Radiation Oncology, University of California, San Francisco, Comprehensive Cancer Center,  
1600 Divisadero Street, San Francisco, California 94143-1708

Susan Moyher Noworolski and John Kurhanewicz

The Center for Molecular and Functional Imaging, Department of Radiology, University of California,  
San Francisco, 185 Berry Street, Suite 350, San Francisco, California 94143-0946

(Received 8 August 2005; accepted for publication 6 December 2005; published 26 January 2006)

Magnetic resonance imaging (MRI) and magnetic resonance spectroscopic imaging (MRSI) have been shown to be very useful for identifying prostate cancers. For high sensitivity, the MRI/MRSI examination is often acquired with an endorectal probe that may cause a substantial deformation of the prostate and surrounding soft tissues. Such a probe is removed prior to radiation therapy treatment. To register diagnostic probe-in magnetic resonance (MR) images to therapeutic probe-out MR images for treatment planning, a new deformable image registration method is developed based on biomechanical modeling of soft tissues and estimation of uncertain tissue parameters using nonlinear optimization. Given two-dimensional (2-D) segmented probe-in and probe-out images, a finite element method (FEM) is used to estimate the deformation of the prostate and surrounding tissues due to displacements and forces resulting from the endorectal probe. Since FEM requires tissue stiffness properties and external force values as input, the method estimates uncertain parameters using nonlinear local optimization. The registration method is evaluated using images from five balloon and five rigid endorectal probe patient cases. It requires on average 37 s of computation time on a 1.6 GHz Pentium-M PC. Comparing the prostate outline in deformed probe-out images to corresponding probe-in images, the method obtains a mean Dice Similarity Coefficient (DSC) of 97.5% for the balloon probe cases and 98.1% for the rigid probe cases. The method improves significantly over previous methods ( $P < 0.05$ ) with greater improvement for balloon probe cases with larger tissue deformations. © 2006 American Association of Physicists in Medicine. [DOI: 10.1118/1.2163391]

Key words: deformable image registration, prostate finite element model, registration, nonlinear image warping, prostate therapy

## I. INTRODUCTION

Prostate cancer kills over 30 000 Americans each year.<sup>1</sup> It is the second leading cause of cancer death for men in the United States. Recent advances in medical imaging and radiation therapy have the potential to improve patient care by noninvasively identifying the location and extent of prostate cancer and by allowing physicians to target radiation dose to the cancerous lesion while sparing surrounding healthy tissues.

In 1996, Kurhanewicz *et al.* showed that magnetic resonance spectroscopic imaging (MRSI), a type of functional imaging that measures the concentration of metabolic compounds, can be used to noninvasively diagnose and locate cancerous tumors in the prostate.<sup>2-5</sup> By measuring choline, polyamine, and citrate levels that change with the evolution

and progression of cancer, MRSI can be used to identify the location and extent of dominant intraprostatic lesions (DIL's) in the prostate.<sup>6</sup> Combining magnetic resonance imaging (MRI) with MRSI allows the identification of a tumor with specificity of up to 91%.<sup>5</sup>

Pouliot *et al.* integrated MRI/MRSI with treatment planning for high dose rate (HDR) brachytherapy,<sup>7</sup> a type of radiotherapy used for treating prostate cancer, where radioactive sources are placed in close proximity to cancerous tumors. In HDR, an afterloader moves a single radioactive source (<sup>192</sup>Ir) of length 4.5 mm and diameter 0.9 mm along 16 to 18 catheters temporarily implanted inside the prostate. By adjusting the length of time (dwell time) that the source remains at any location (dwell position) within a catheter, it is possible to generate and optimize over a wide variety of dose distributions.<sup>8</sup> Combined MRI/MRSI allows physicians

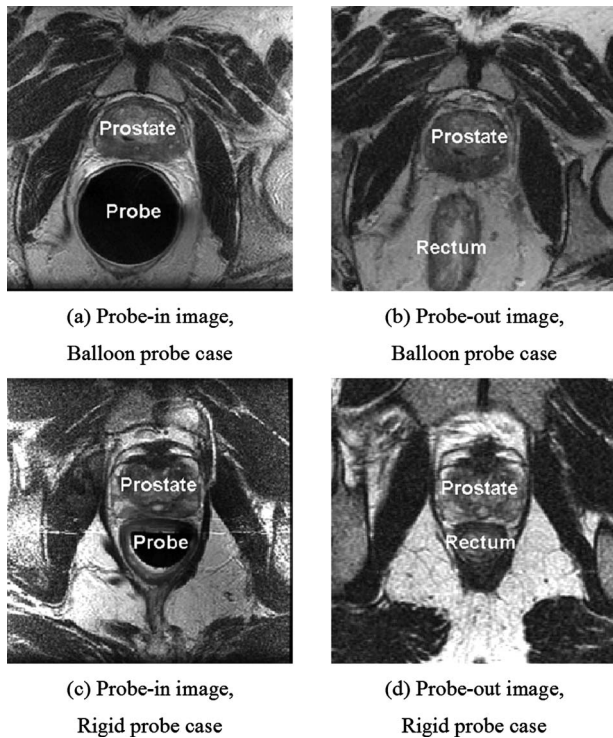


FIG. 1. MRSI data is obtained with a balloon endorectal probe inserted and inflated (a) or a rigid endorectal probe (c), as shown in the axial MR images at the midgland of the prostate. Radiation treatment is performed with the probe removed (b), (d).

to escalate dose for the DIL.<sup>7</sup> Dose escalation for DIL's identified using MRI/MRSI has also been applied to external beam radiation treatment<sup>9,10</sup> and permanent seed implants.<sup>11</sup>

To obtain an improved signal-to-noise ratio (SNR) and better spatial resolution MRI and MRSI, an endorectal probe integrated with a pelvic phased array (PPA) coil is commonly used. The endorectal probe is critical for the acquisition of high spatial resolution ( $\approx 0.3 \text{ cm}^3$ ) MRSI data of the prostate due to the approximate ten-fold increase in SNR relative to external phased array coils.<sup>3-5,12-14</sup> However, the probe may cause considerable nonlinear translation and distortion of the prostate,<sup>15</sup> as shown in Fig. 1. The probe is generally removed during imaging for radiation treatment planning and therapy. We present an image registration algorithm that compensates for tissue deformations to map MRSI data from the probe-in image to a probe-out image.

To register probe-in images obtained during a combined MRI/MRSI staging examination to probe-out images, we developed a 2-D finite element based model that estimates the deformation of the prostate and surrounding tissues in the plane of the image due to the insertion of an endorectal probe. A 2-D model is sufficient for our application since the out-of-plane deformations are smaller than the thickness of imaging slices.<sup>15,16</sup> A key problem with any biomechanical model is that patient-specific model parameters required as input are not known with certainty, including tissue stiffness properties for the prostate and surrounding soft tissues. Additional uncertain parameters include forces due to patient position changes, bladder volume changes, and other factors

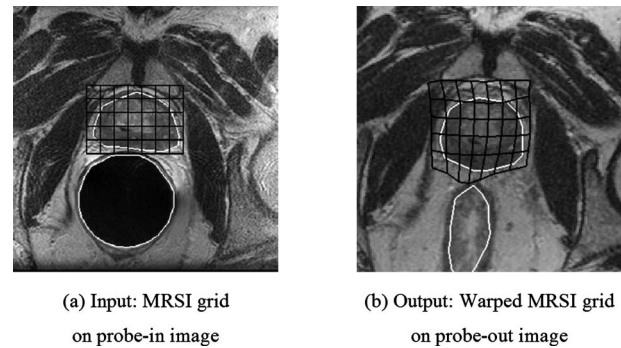


FIG. 2. Spectroscopy data is obtained for voxels inside the MRSI grid overlaid on an the axial probe-in MR image (a). Our image registration method warps the MRSI grid to the probe-out image for use during treatment planning (b).

that differ between the probe-out and probe-in images but are not explicitly included in our linear elasticity soft tissue deformation model. We use a local nonlinear optimization algorithm to estimate uncertain patient-specific tissue stiffness properties and external forces to maximize image registration quality. Compensating for computed tissue deformations results in a nonlinear warping of the MRSI grid, as shown in Fig. 2.

Past work on image registration of the prostate includes rigid transformations,<sup>17,15</sup> spline transformations,<sup>18,19</sup> energy models,<sup>20</sup> and finite element models<sup>21-23</sup> for registering dose calculation CT images,<sup>21</sup> treatment and interventional MR images,<sup>17,18,22</sup> probe-in/probe-out MR images,<sup>23</sup> and MR images with endorectal balloons at different levels of inflation.<sup>20</sup> Fei *et al.* ignore tissue deformations that occur between pre-operative and interventional MR images and maximize the mutual information (MI) or correlation coefficient (CC) of the image intensity histograms using rigid body translation and rotation of the prostate.<sup>17</sup> Kim *et al.* rigidly align probe-in and probe-out images by first rotating the images into the same plane, then doing a rigid 2-D translation in plane.<sup>15</sup> For a sample probe-in/probe-out case in which prostate deformation is minimal, this method achieves less than 2 mm registration error. Fei *et al.* and Kessler *et al.* use spline methods, which nonlinearly warp an image using a nonphysically based model with a large number of degrees of freedom.<sup>18,19</sup> They use multiresolution approaches to increase the avoidance of local maxima of the CC and MI metrics. Wu *et al.* develop a hybrid method for registering MR images with endorectal balloons at different levels of inflation by maximizing an objective function containing a weighted sum of MI and regularization energy from a non-finite element physically based model.<sup>20</sup> A key advantage of these methods based on MI and CC quality metrics is that tissue segmentation is not required, but these methods have large numbers of degrees of freedom, are prone to local maxima, require long computation times (18–22 min for Wu *et al.*), and have potentially larger error due to soft boundaries of deformable tissues.<sup>17,20</sup> MI and CC metrics cannot be applied in isolation to our problem of registering a probe-in image to a probe-out image because, without segmentation,

the probe-out image contains no information on the probe insertion location. Physically based biomechanical models, such as the finite element method, have the potential to address some of these limitations. Finite element methods require image segmentation to define tissue type boundaries (to specify tissue-specific material properties) and mesh generation. Yan *et al.* performed pioneering work in deformable image registration based on the finite element method to calculate fractionated dose in a deforming organ.<sup>21</sup> They segmented a single tissue type, the rectal wall, and applied the method to intertreatment motion using fiducials to set boundary conditions. Bharatha *et al.* and Crouch *et al.* apply linear elasticity finite element modeling to the prostate using a tetrahedral mesh with distinct central gland and peripheral zone regions<sup>22</sup> and a hexahedral mesh using a medially based solid representation with uniform tissue properties inside the prostate.<sup>23</sup> Image registration based on biomechanical models, including finite element and energy methods, require tissue material properties as input. In past work we are aware of, material properties are either fixed as constants for all patients<sup>21–23</sup> or implicitly held constant across an entire image.<sup>20</sup> Our image registration method uses nonlinear optimization to set patient-specific values for uncertain parameters in the biomechanical model including separate tissue stiffness values for each segmented tissue type. We also explicitly warp MRSI grids to compensate for tissue deformations. This paper is a revised and extended version of preliminary ideas presented in 2004.<sup>24</sup>

## II. METHODS AND MATERIALS

### A. Patient image acquisition

We applied our image registration method retrospectively to ten patient cases. The patients were recruited from January to June, 2003, at the Magnetic Resonance Science Center (MRSC), University of California, San Francisco. A balloon probe (USA Instruments, Aurora, OH) with 100 cc of air injected was used for five patients while a rigid probe (MedRad, Pittsburgh, PA) was used for the remaining five patients. Once inflated, the balloon probe had a circular cross section with a 48 mm diameter. The rigid probe was a half ellipse, in cross section, with the anterior surface flat. Its right–left extent was 29 mm and its anterior–posterior extent was 16.5 mm. Combined MRI/MRSI was obtained using the balloon or rigid probe in combination with an external phased array of coils on a 1.5 Tesla GE system (Signa, GE Medical Systems, Milwaukee, WI). For rigid probe cases, the USA torso phased array was used, while the GE pelvic phased array was used for the balloon probe cases. These two probes were selected as the MedRad coil is the only MR probe currently available commercially and the USA Instruments probe is commercially manufactured and will soon be a commercially available alternative probe.

The probe-in images used in this study were acquired during a “PROSE” (PROstate Spectroscopy and imaging Examination) MRI/MRSI examination (GE Medical Systems, Milwaukee, WI). The details of the MR imaging method used have been discussed in previous work.<sup>3,7,15,25</sup> Spectros-

copy data was obtained for  $7 \times 7 \times 7$  mm voxels ( $\approx 0.3 \text{ cm}^3$ ). Thin section high spatial resolution axial  $T_2$ -weighted fast spin-echo images of the prostate and seminal vesicles were obtained with a slice thickness of 3 mm, an interslice gap of 0 mm, and a field of view (FOV) of 14 cm. At the end of the “PROSE” MRI/MRSI examination, the endorectal probe was removed, with the subject remaining on the imaging table. Additional sagittal and axial fast spin echo  $T_2$ -weighted images were acquired without the endorectal probe using the phased array coil alone for signal reception. As with the probe-in case, patients were scanned in the supine position. All image acquisition parameters for the probe-out images were the same as for the probe-in images except for increasing the field-of-view (FOV) from 14 to 20 cm to partially compensate for the reduction in SNR obtained without the use of an endorectal probe.

### B. Image registration method overview

Our image registration method, which applies to planar slices of tissue, defines a mapping  $F$  between a probe-out image and a probe-in image. The mapping  $F$  represents the deformation of the prostate and surrounding tissue due to endorectal probe insertion. Given a probe-out image  $A$  and a probe-in image  $B$ , the goal is to compute  $F$  such that  $F(A) = B$ . The inverse mapping  $F^{-1}$ , which can be used during treatment planning, transforms every point in the MRSI grid of the probe-in image  $B$  to its coordinate in the probe-out image  $A$ .

At the core of our method to compute  $F$  is a 2-D finite element model that estimates the deformation of soft tissues in the probe-out image due to insertion of the endorectal probe. Treating the uncertain tissue stiffness properties and external forces as unknown variables, we estimate their values using nonlinear local optimization to maximize image registration quality. Our current optimization routine includes 3 uncertain stiffness parameters and between 20 and 40 external forces applied on the prostate boundary, each with 2 degrees of freedom.

To quantify the accuracy of the image registration, we measure the overlap between the prostate area in the probe-in image  $B$  and the prostate area in the deformed probe-out image  $F(A)$  using the Dice Similarity Coefficient (DSC). Superimposing an outlined area from two images, the DSC is defined as

$$D = \frac{2a}{2a + b + c},$$

where  $a$  is the number of picture elements (pixels) shared by both areas,  $b$  is the number of pixels unique to the first area, and  $c$  is the number of pixels unique to the second area.<sup>26,22</sup> The DSC is a scalar between 0 and 1, with higher values representing better quality registration.

### C. Method input

The input for our image registration method is a segmented probe-in image and a segmented probe-out image.

From the probe-in and probe-out MR image volumes, we selected a single probe-in image slice at the midland of the prostate for each patient. We then manually selected a corresponding probe-out image slice that is at the same level as the probe-in image for the patient. We align rigid points in the images, such as points in bones, using a homologous point method to translate the images.<sup>27</sup>

We manually segmented the selected images using a standard image segmentation method by drawing polygonal outlines on a computer screen to define the boundaries of tissue types. For cases in which the tissue type (such as the rectum) was close to circular, we specified a circle and radius that the software automatically converted to a polygonal approximation. The image registration method requires segmentation of the probe and prostate in the probe-in image and the probe entry location (rectum) and prostate in the probe-out image. For improved accuracy in the biomechanical simulation, we also segmented bones and separately segmented the central gland (CG) and peripheral zone (PZ) of the prostate in the probe-out image. Additional segmentation of the probe-in image will not improve results since the biomechanical model is applied to deform the probe-out image.

Our image registration method is sensitive to the segmentation of the image and the optimization algorithm may incorrectly add external forces or modify tissue stiffness properties if the segmentation is incorrect. Bhathara *et al.* quantified the error introduced by human segmentation: a human subject segmenting five 1.5 T MRI scans five times in random order achieved a mean DSC for segmentation reproducibility of 95% with a 95% confidence interval of (92%, 97%) while a second subject achieved a mean of 96% with confidence interval (95%, 97%).<sup>22</sup>

#### D. Finite element model of soft tissue deformations

We approximate tissues as nearly incompressible (Poisson's ratio of 0.49), linearly elastic, and isotropic. Although tissue stiffness properties will be modified during the optimization method, initial default values must be set. Based on tissue stiffness measurements obtained using ultrasound elastography in previous work,<sup>28</sup> we temporarily assign a Young's modulus of 60 kPa to the central gland of the prostate and 30 kPa to all surrounding tissues for all patient images. We assume initial external forces all have zero magnitude.

We automatically generate a finite element mesh composed of  $n=500$  nodes and between 800 and 1000 triangular elements that conform to the polygonal segmented tissue type boundaries using the constrained Delaunay triangulation software program *Triangle*.<sup>29</sup> Image segmentation and the mesh generated for the probe-out image of a sample case are shown in Fig. 3. Elements in the mesh are assigned default stiffness properties based on tissue type. Mesh nodes defining elements inside bones are constrained to be fixed.

As shown in Fig. 4, our model expands the rectum lining in the probe-out image to match the probe outline in the probe-in image. We project probe-out image mesh nodes along the ray based at the rectum center and constrain them

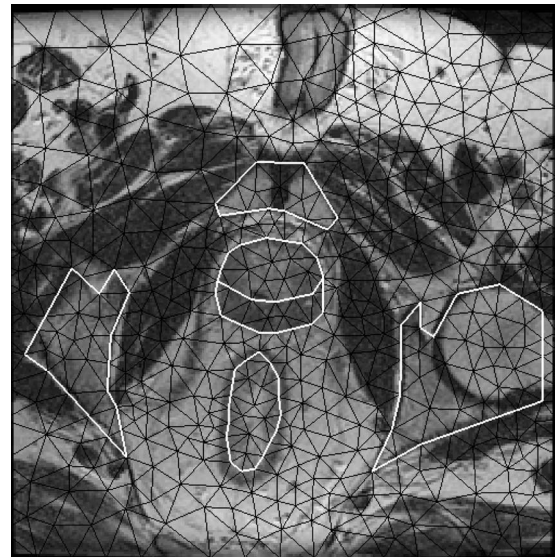


FIG. 3. Conformal Delaunay triangular mesh (black triangles) for a probe-out image with central gland and peripheral zone of the prostate, probe entry location (rectum), and bones segmented (in white).

to the intersection with the probe-in image probe outline. The deformations of the surrounding soft tissues, including the prostate, are computed using a 2-D finite element method (FEM). The FEM problem for a given probe-out image mesh with  $n$  nodes is defined by a system  $\mathbf{K}\mathbf{u}=\mathbf{f}$  containing  $2n$  linear equations, where  $\mathbf{K}$  is the global stiffness matrix,  $\mathbf{f}$  is the external force vector, and  $\mathbf{u}$  is the nodal displacement vector.<sup>30</sup> For each fixed node, we remove its two corresponding degrees of freedom from the system. We solve the linear system of equations numerically using the Gauss-Seidel method to compute nodal displacements  $\mathbf{u}$  for nonfixed nodes. By using linear interpolation within each element of the mesh, the nodal displacement vector  $\mathbf{u}$  defines a complete invertible mapping function  $F$  between the probe-out image and the corresponding probe-in image.

The mapping  $F$  is applied to every element in the probe-out image  $A$  to obtain the deformed probe-out image  $F(A)$ , as shown in Fig. 4. Rendering the deformed probe-out image is performed quickly using texture mapping, which is built in

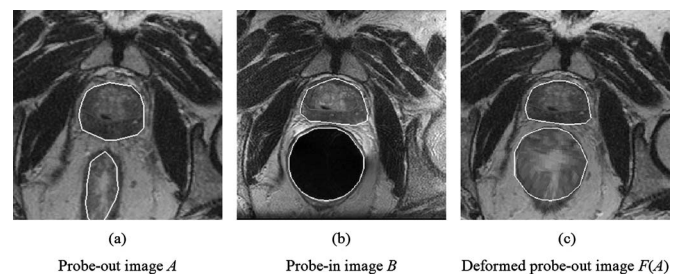


FIG. 4. Probe-out image  $A$  with segmented prostate gland (outlined in white, middle) and rectum (outlined in white, bottom) (a) and the corresponding probe-in image  $B$  with prostate and probe segmented (b). The method computes image  $F(A)$  (c), which displaces mesh nodes along the rectum in the probe-out image to the probe outline in the probe-in image and estimates the resulting soft tissue deformations. The image registration quality (DSC value) between (b) and (c) is 97.8%.

TABLE I. DSC mean and standard deviation (in parentheses) for image registration quality.

	Rigid translation	Our method
Five balloon probe cases	86.6% (10.4%)	97.5% (0.7%)
Five rigid probe cases	94.1% (2.7%)	98.1% (0.4%)

to most modern computer graphics cards. The quality of the mapping  $F$  is determined by how closely the deformed probe-out image  $F(A)$  matches the probe-in image  $B$ . We use the DSC quality metric defined in Sec. II B to quantify the similarity between  $F(A)$  and  $B$  by measuring the overlap of prostate area.

### E. Optimization of uncertain parameters

Our image registration method treats tissue stiffness properties and external forces at mesh nodes along the prostate boundary as uncertain parameters. Tissue stiffness is constrained between 1 and 600 kPa. External force magnitudes are unbounded. We define the optimization objective function for maximization as

$$Q = D - \alpha E,$$

where  $D$  is the DSC for the prostate,  $\alpha$  is a scaling parameter, and  $E$  is the percent of strain energy due to external forces. To compute  $E$ , the optimization algorithm computes tissue deformations twice, first without external forces and then with external forces added. For each case, it computes the total strain by summing the strain of each element in the mesh, which is quickly computed by multiplication of element stiffness matrices and vectors of node displacements.<sup>30</sup> We subtract  $\alpha E$  in the objective function to prioritize optimization of parameters of the physically based model (tissue stiffness) relative to external forces. Appropriately setting  $\alpha$ , as described in Secs. II G and III, produces visually smoother image mappings by preventing unrealistic large magnitude external forces.

We apply the Steepest Descent method with Armijo's Rule for a line search<sup>31</sup> to maximize the nonlinear objective function  $Q$ . The variables, which include  $m=3$  tissue stiffness properties and  $l \approx 60$  external force degrees of freedom depending on the mesh, are defined in a vector  $\mathbf{x}$  of dimension  $m+l$ . The quality metric  $Q$  is a function  $Q(\mathbf{x})$ . We numerically compute derivatives for the gradient  $\nabla Q(\mathbf{x})$  using finite differences with sufficiently high differences to avoid

numerical difficulties. At iteration  $i$  of the Steepest Descent optimization method, Armijo's Rule selects the next candidate point  $\mathbf{x}_{i+1} = \mathbf{x}_i + 2^t \lambda \nabla Q(\mathbf{x}_i)$  for predefined step size  $\lambda$  by sequentially incrementing integer  $t$  starting at  $t=0$  to solve for the maximum  $t$  that improves  $Q(\mathbf{x}_{i+1})$ . Then the gradient  $\nabla Q(\mathbf{x}_{i+1})$  is computed and the Steepest Descent algorithm repeats until iteration  $j$ , where  $\|\nabla Q(\mathbf{x}_j)\| < \epsilon$  for  $\epsilon=0.001$ . Because the objective function  $Q$  is not guaranteed to be convex, this method may not find a global optimal solution.<sup>31</sup>

### F. Warping the MRSI grid

The 3-D MRSI data is collected from a volume and individual spectra are generally reconstructed for  $7 \times 7 \times 7$  mm voxels within a grid overlaid on this volume. To help register spectroscopic data to the probe-out image, we transform each intersection point in the regular MRSI grid from the probe-in image plane to the probe-out image using the inverse of mapping  $F$ . The warped MRSI grid is the output of the algorithm: it registers the probe-in MRSI data to a probe-out image for use during treatment planning.

### G. Method evaluation and parameter selection

We evaluate the image registration method using two metrics: DSC and point error. We compute the DSC using the prostate outline in the probe-in image  $B$  and the prostate outline in the deformed probe-out image  $F(A)$ . We compare our deformable image registration method to a rigid registration method where the center of mass of the prostate total gland is translated in the probe-out image by the distance between its center of mass in the probe-out and probe-in images.<sup>22</sup>

As a second measure of image registration quality, we evaluate displacement errors of homologous points in the interior of the prostate on the probe-in images  $B$  and the deformed probe-out images  $F(A)$ . As in past work by Bharatha *et al.*,<sup>22</sup> we selected points on the probe-in images at the posterior border of the central gland near the midline of the prostate. We then selected homologous points corresponding to the same tissue location on the probe-out images using patient-specific local image pixel intensity variations as references. Our image registration method maps the point on the probe-out image  $A$  to the deformed probe-out image  $F(A)$  so we can directly measure the point error: the distance between the homologous point in  $B$  and  $F(A)$ . We compare this error to the distance between the homologous points in the

TABLE II. Point displacement error means and standard deviations (in parentheses) for sample homologous points on the boundary of the prostate central gland and peripheral zone near the midline.

	Mean point error for probe-in/ probe-out images (mm)	Mean point error after our method (mm)	Mean reduction in error (%)
Five balloon probe cases	9.22 (3.22)	1.95 (0.22)	74.8% (15.1%)
Five rigid probe cases	3.93 (1.59)	0.97 (0.51)	70.0% (27.2%)

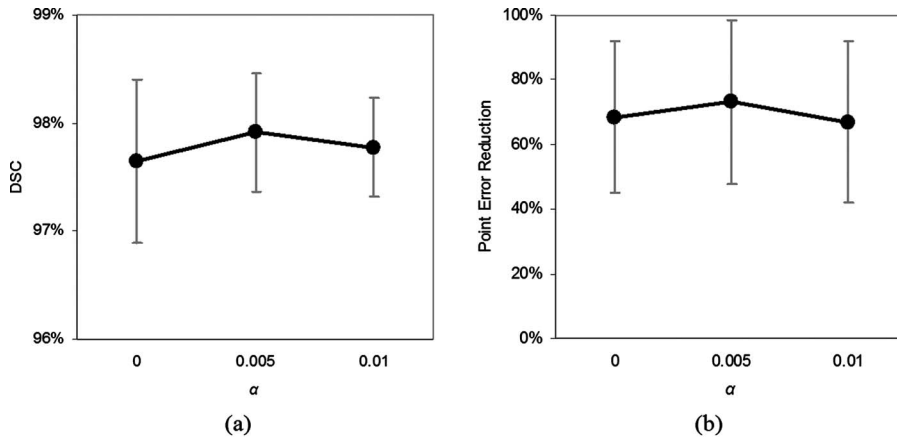


FIG. 5. Sensitivity of mean image registration quality (DSC and point errors) to the optimization parameter  $\alpha$ , with errors bars for standard deviations.

given probe-in image  $B$  and probe-out image  $A$  to quantify the registration improvement resulting from the method.

Two parameters of the method that influence image registration quality and must be set are  $n$ , the number of nodes in the mesh, and  $\alpha$ , the scaling parameter in the objective function  $Q$  that weighs direct maximization of the DSC relative to the percent of strain energy  $E$  due to external forces. For a subset of the patient data (three balloon probe cases and three rigid probe cases), we evaluated image registration quality for  $n=100, 500$ , and  $1000$  and for  $\alpha=0.0, 0.005$ , and  $0.01$ .

### III. RESULTS

The mean DSC of our method was 97.5% with a standard deviation of 0.7% for the 5 balloon probe cases. For the 5 rigid probe cases, the mean DSC was 98.1% with a standard deviation of 0.4%. As shown for a patient case in Fig. 4, the deformed probe-out image closely matches the probe-in image. In Table I, we compare our image registration method to rigid registration based on center-of-mass translation for the prostate total gland. We performed paired  $t$  tests to determine the statistical significance ( $P < 0.05$ ) of the results and found that the improvement in DSC using our method was statistically significant for both the balloon probe ( $P=0.035$ ) and the rigid probe ( $P=0.013$ ) cases.

The results of our method for the point error metric are shown in Table II. Our method reduces displacement error between the homologous points in the probe-in and probe-

out images by a mean of 74.8% to a mean error of 1.95 mm for the balloon probe cases. For the rigid probe cases, the reduction was by a mean of 70.0% to a mean error of 0.97 mm. We performed paired  $t$  tests and found that the reduction in error was statistically significant for both the balloon probe ( $P=0.0045$ ) and the rigid probe ( $P=0.0099$ ) cases.

For these results, we set parameter  $\alpha$  in the formula for objective function  $Q$  in Sec. II E to 0.005. Decreasing  $\alpha$  allows for greater external forces while increasing  $\alpha$  penalizes external forces in favor of tissue stiffness during the optimization of uncertain parameters. The trade-off effect of  $\alpha$  on DSC and point error is shown in Figs. 5(a) and 5(b). Increasing  $\alpha$  to 0.01 or decreasing  $\alpha$  to 0.0 results in lower mean DSC and higher mean point errors.

We also performed a sensitivity analysis on  $n$ , the number of nodes in the finite element mesh. Increasing  $n$  improves average image registration quality measured by DSC, as shown in Fig. 6(a). However, this improvement comes at a large computation cost, as shown in Fig. 6(b), with 1000 node meshes requiring over 6 min of computation time on average. Results in this study use meshes with  $n=500$  nodes, which requires less than 1 min of computation time per image slice while maintaining good image registration quality; DSC results with  $n=500$  are not significantly different from DSC results with  $n=1000$  ( $P=0.324$ ).

We show the output of our image registration method for a sample balloon probe patient in Fig. 7 and for a rigid probe

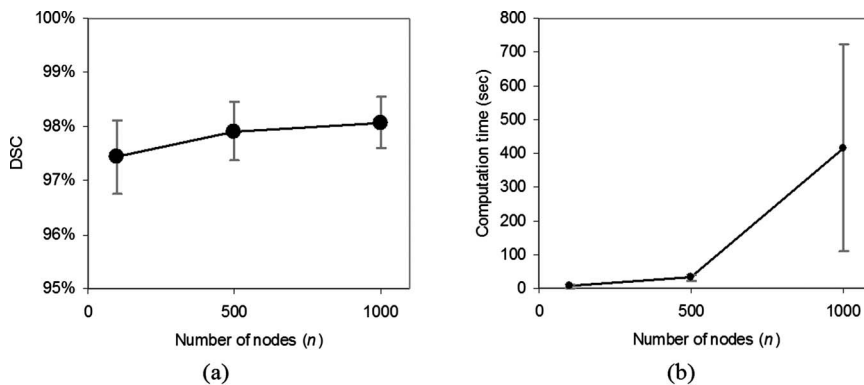


FIG. 6. Sensitivity of mean DSC image registration quality (a) and computation time (b) to the number of nodes  $n$  in the mesh, with error bars for standard deviations.

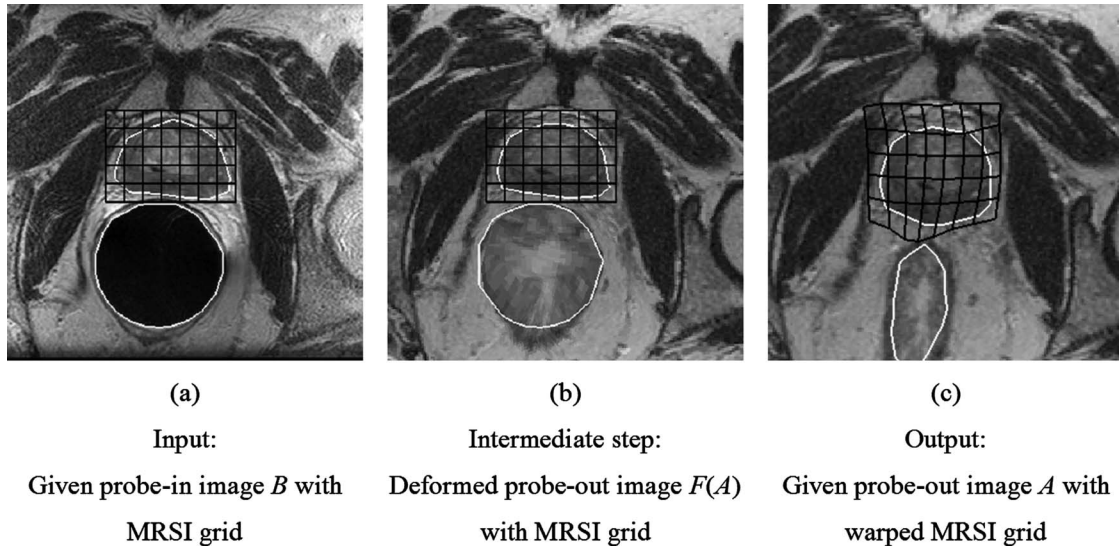


FIG. 7. Sample balloon probe case. A comparison of input and output images shows the nonlinear warping of the MRSI grid. The probe-in image (a) closely matches the computed deformed probe-out image (b) outside the endorectal probe. The MRSI grid is warped to the undeformed probe-out image (c) for use during treatment planning.

patient in Fig. 8. The resulting warping of the MRSI grid is clearly nonlinear in both cases. The percentage of strain energy due to external forces  $E$  averaged 8.6% for balloon probe cases and 10.0% for rigid probe cases. The low value for  $E$  demonstrates that, for both types of probes, most of the strain energy in the finite element simulation was due directly to the displacement of tissues caused by the probe rather than other uncertain external forces. The mean computation time for the image registration algorithm was comparable for both balloon and rigid probe patients on a 1.6 GHz Pentium-M laptop PC: 39.8 s with a standard deviation of 20.8 s for balloon probe cases and 34.2 s with a standard deviation of 11.8 seconds for rigid probe cases.

#### IV. DISCUSSION

Compensating for tissue deformations using biomechanical simulation with nonlinear parameter estimation results in better image registration than center-of-mass translation for all of the ten cases tested. The DSC increased by an average 7.5% across all patients when using our method. These improvements come at a cost of computation time: our method required, on average, 37 s for each patient image slice in addition to manual image segmentation time for the probe-in and probe-out images.

Since our method only explicitly considers deformation in a 2-D  $(x, y)$  plane, it will not address out-of-plane deforma-

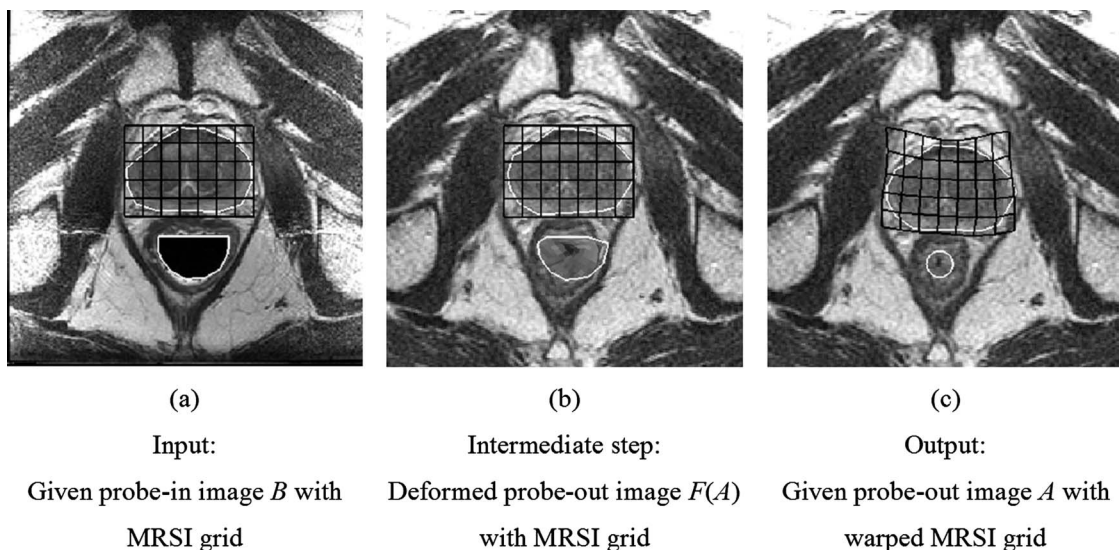


FIG. 8. Sample rigid probe case.

tions along the  $z$  axis in a 3-D volume. However, past work has shown that  $z$ -axis deformations are small relative to the resolution of the volume images. Kim *et al.* found that the difference in the superior/inferior length of the prostate between probe-in and probe-out images was always less than the  $z$ -axis thickness of an axial MR image (3 mm) for 25 patient cases (15 rigid probe and 10 balloon probe).<sup>15</sup> Crouch *et al.* measured seed displacements for 25 implanted seeds between balloon probe-in and probe-out images and found that the  $z$ -axis displacement averaged 2.67 mm, less than the 3 mm MR image slice thickness.<sup>16</sup>

Using our method for image registration resulted in a greater improvement in mean DSC for balloon probe images (10.9%) than for rigid probe images (4.0%) when compared to registration by center-of-mass translation. Although balloon probes result in better quality images, these probes produce much larger deformations.<sup>15</sup> Kim *et al.* manually measured the anterior–posterior (AP) and right–left (RL) dimensions of the prostate in probe-in and probe-out images and found that the balloon probes, on average, compressed the prostate 3.5-fold more in the AP direction and stretched the prostate 2.5-fold more the RL direction than the rigid probe.<sup>15</sup>

When compared to other image registration methods based on tissue deformation models, our method performs well. Our results visually appear to have smaller error than results from 2-D slices of 3-D volumes obtained by Wu *et al.*, although a precise comparison is not possible because the accuracy of their method was not numerically quantified.<sup>20</sup> Wu *et al.* consider images taken with a balloon probe at different levels of inflation, which results in different deformations from removing the probe entirely for a probe-out image. Crouch *et al.* tested their finite element-based method using an artificial tissue phantom with 25 radioactive seeds implanted inside.<sup>16,23</sup> The phantom was deformed by a balloon probe resulting in average seed displacements of 9.377 mm, similar to the 9.22 mm average displacement of our test points in the interior of the prostate. To achieve 2.0 mm average point errors for the seeds, Crouch *et al.* required a mesh of 14 068 nodes and 14 h of computation time for full 3-D deformations. Our method, which was tested on MR images of patient cases rather than tissue phantoms, achieved a less than 2 mm error for a representative point but required under 1 min of computation time per image slice. Our DSC of 97.5% is higher than the 94% obtained by Bharatha *et al.* with a 3-D biomechanical finite element model for the registration of balloon endorectal probe-in images to rectal obturator (smaller) probe images.<sup>22</sup> However, subjects in that study were scanned in two different positions, supine and lithotomy, at two different field strengths, 1.5 and 0.5 T, and with two different rectal probes, an MR expandable endorectal probe and a rectal obturator, which may have compromised image registration quality.

## V. CONCLUSION

Biomechanical modeling with nonlinear estimation of uncertain tissue parameters can improve the quality of registra-

tion of (probe-in) MRSI data for (probe-out) radiation treatment planning. Improvements in image registration quality are greater for balloon probes compared to rigid probes due to the larger tissue deformations that occur with balloon probes. The algorithm achieved a mean DSC quality of 97.5% for five balloon probe patients and 98.1% for five rigid probe patients. The improvement over center-of-mass rigid registration is statistically significant ( $P < 0.05$ ). Our method reduced displacement error between homologous test points in the probe-in and probe-out images by a mean 74.8% to a mean error of 1.95 mm for balloon probe cases and by a mean 70.0% to a mean error of 0.97 mm for rigid probe cases. The method required, on average, 37 s of computation time on a 1.6 GHz Pentium-M laptop PC to estimate and compensate for tissue deformations and produce a non-linear mapping between probe-in and probe-out images.

Our current method independently registers 2-D slices of tissue from a 3-D MRI volume. We are currently developing an analogous 3-D biomechanical simulation and image registration method to explicitly account for deformations and displacements that occur between imaging planes in 3-D volumes. Generating patient-specific 3-D conformal tetrahedral meshes with a controlled number of elements and validating the 3-D image registration approach using a new imaging protocol with slices sufficiently thin to capture out-of-plane deformations will require substantial new research. We also plan to extend the method to register deformations that occur due to catheter insertion for HDR brachytherapy treatment planning, which will also require a new imaging dataset and new models of forces exerted by the catheters on soft tissue.

## ACKNOWLEDGMENTS

This work was supported in part by the National Institutes of Health under Grant No. R21 EB003452 and by a National Science Foundation Graduate Research Fellowship to Ron Alterovitz. We also thank Michael Yu and Michael Wehner at UC Berkeley for their help and advice.

<sup>a)</sup> Author to whom correspondence should be addressed. Department of Industrial Engineering and Operations Research, University of California, Berkeley, 4141 Etcheverry Hall, Berkeley, California 94720-1777. Telephone: (510) 643-2030; fax: (510) 642-1403; electronic mail: ron@ieor.berkeley.edu

<sup>1</sup> National Center for Health Statistics, "Prostate disease." Available at <http://www.cdc.gov/nchs/fastats/prostate.htm>

<sup>2</sup> J. Kurhanewicz, H. Hricak, D. B. Vigneron *et al.*, "Prostate cancer: Metabolic response to cryosurgery as detected with 3D H-1 MR spectroscopic imaging," *Radiology* **200**, 489–496 (1996).

<sup>3</sup> J. Kurhanewicz, D. B. Vigneron, H. Hricak *et al.*, "Three-dimensional H-1 MR spectroscopic imaging of the *in situ* human prostate with high (0.24–0.7-cm<sup>3</sup>) spatial resolution," *Radiology* **198**, 795–805 (1996).

<sup>4</sup> J. Kurhanewicz, D. Vigneron, and S. J. Nelson, "Three-dimensional magnetic resonance spectroscopic imaging of brain and prostate cancer," *Neoplasia* **2**, 166–189 (2000).

<sup>5</sup> J. Scheidler, H. Hricak, D. B. Vigneron *et al.*, "Prostate cancer: Localization with three-dimensional proton MR spectroscopic imaging—clinicopathologic study," *Radiology* **213**, 473–480 (1999).

<sup>6</sup> J. Kurhanewicz, M. Swanson, S. J. Nelson, and D. Vigneron, "Combined magnetic resonance imaging and spectroscopic imaging approach to molecular imaging of prostate cancer," *J. Magn. Reson Imaging* **16**, 451–463 (2002).

<sup>7</sup> J. Pouliot, Y. Kim, E. Lessard, I. C. Hsu, D. Vigneron, and J.

- Kurhanewicz, "Inverse planning for HDR prostate brachytherapy use to boost dominant intra-prostatic lesion defined by magnetic-resonance spectroscopy imaging," *Int. J. Radiat. Oncol., Biol., Phys.* **59**, 1196–1207 (2004).
- <sup>8</sup>E. Lessard and J. Pouliot, "Inverse planning anatomy-based dose optimization for HDR-brachytherapy of the prostate using fast simulated annealing algorithm and dedicated objective function," *Med. Phys.* **28**, 773–779 (2001).
- <sup>9</sup>B. Pickett, E. Vigneault, J. Kurhanewicz, L. Verhey, and M. Roach, "Static field intensity modulation to treat a dominant intraprostatic lesion to 90 Gy compared to seven field 3-dimensional radiotherapy," *Int. J. Radiat. Oncol., Biol., Phys.* **43**, 921–929 (1999).
- <sup>10</sup>P. Xia, B. Pickett, E. Vigneault, L. Verhey, and M. Roach, "Forward or inversely planned segmental multileaf collimator IMRT and sequential tomotherapy to treat multiple dominant intraprostatic lesions of prostate cancer to 90 Gy," *Int. J. Radiat. Oncol., Biol., Phys.* **51**, 244–254 (2001).
- <sup>11</sup>M. Zaider, M. J. Zelefsky, E. K. Lee *et al.*, "Treatment planning for prostate implants using magnetic-resonance spectroscopy imaging," *Int. J. Radiat. Oncol., Biol., Phys.* **47**, 1085–1096 (2000).
- <sup>12</sup>H. Hricak, S. White, D. Vigneron, J. Kurhanewicz, A. Kosco, D. Levin, J. Weiss, P. Narayan, and P. R. Carroll, "Carcinoma of the prostate gland: MR imaging with pelvic phased-array coils versus integrated endorectal—pelvic phased-array coils," *Radiology* **193**, 703–709 (1994).
- <sup>13</sup>C. E. Hayes, M. J. Dietz, B. F. King, and R. L. Ehman, "Pelvic imaging with phased array coils: quantitative assessment of signal-to-noise ratio improvement," *J. Magn. Reson.* (1969-1992) **2**, 321–326 (1992).
- <sup>14</sup>J. E. Husband, A. R. Padhani, A. D. MacVicar, and P. Revell, "Magnetic resonance imaging of prostate cancer: comparison of image quality using endorectal and pelvic phased array coils," *Clin. Radiol.* **53**, 673–681 (1998).
- <sup>15</sup>Y. Kim, I. C. Hsu, J. Pouliot, S. M. Noworolski, D. B. Vigneron, and J. Kurhanewicz, "Expandable and rigid endorectal coils for prostate MRI: Impact on prostate distortion and rigid image registration," *Med. Phys.* **32**, 3569–3578 (2005).
- <sup>16</sup>J. R. Crouch, "Medial techniques for automating finite element analysis," Ph.D. thesis, University of North Carolina, Chapel Hill, 2003.
- <sup>17</sup>B. Fei, A. Wheaton, Z. Lee, J. I. Duerk, and D. Wilson, "Automatic MR volume registration and its evaluation for the pelvis and prostate," *Phys. Med. Biol.* **47**, 823–838 (2002).
- <sup>18</sup>B. Fei, C. Kemper, and D. L. Wilson, "A comparative study of warping and rigid body registration for the prostate and pelvic MR volumes," *Comput. Med. Imaging Graph.* **27**, 267–281 (2003).
- <sup>19</sup>M. Kessler, M. Roberson, R. Zeng, and J. Fessler, "Deformable image registration using multiresolution B-splines," *Med. Phys.* **31**, 1792 (2004) (abstract).
- <sup>20</sup>X. Wu, S. J. Dibiase, R. Gullapalli, and C. X. Yu, "Deformable image registration for the use of Magnetic Resonance Spectroscopy in prostate treatment planning," *Int. J. Radiat. Oncol., Biol., Phys.* **58**, 1577–1583 (2004).
- <sup>21</sup>D. Yan, D. A. Jaffray, and J. W. Wong, "A model to accumulate fractionated dose in a deforming organ," *Int. J. Radiat. Oncol., Biol., Phys.* **44**, 665–675 (1999).
- <sup>22</sup>A. Bharatha, M. Hirose, N. Hata, S. K. Warfield, M. Ferrant, K. H. Zou, E. Suarez-Santana, J. Ruiz-Alzola, A. D'Amico, R. A. Cormack, R. Kininis, F. A. Jolesz, and C. M. C. Tempany, "Evaluation of three-dimensional finite element-based deformable registration of pre- and intraoperative prostate imaging," *Med. Phys.* **28**, 2551–2560 (2001).
- <sup>23</sup>J. R. Crouch, S. M. Pizer, E. L. Chaney, and M. Zaider, "Medially based meshing with finite element analysis of prostate deformation," *Medical Image Computing and Computer-Assisted Intervention, MICCAI 2003-6th International Conference Proceedings, Montreal, Canada, 2003*, pp. 108–115.
- <sup>24</sup>R. Alterovitz, K. Goldberg, J. Kurhanewicz, J. Pouliot, and I. C. Hsu, "Image registration for prostate MR spectroscopy using biomechanical modeling and optimization of force and stiffness parameters," *Proceedings 26th Annual International Conference IEEE Engineering in Medicine and Biology Society*, San Francisco, CA, 2004, pp. 1722–1725.
- <sup>25</sup>"Signa® LX Release 9.1," Chap 6. PROSE Pulse Sequence, 2333956-100 Rev. 0 (05/02), General Electric Company, 2002.
- <sup>26</sup>L. R. Dice, "Measures of the amount of ecologic association between species," *Ecology* **26**, 297–302 (1945).
- <sup>27</sup>R. Horn, "Closed-form solution of absolute orientation using unit quaternions," *J. Opt. Soc. Am. A* **4**, 629–642 (1987).
- <sup>28</sup>T. A. Krouskop, T. M. Wheeler, F. Kallel, B. S. Garria, and T. Hall, "Elastic moduli of breast and prostate tissues under compression," *Ultrasound. Imaging* **20**, 260–274 (1998).
- <sup>29</sup>J. Shewchuk, "Triangle: A two-dimensional quality mesh generator and Delaunay triangulator," <http://www-2.cs.cmu.edu/~quake/triangle.html>, 2003.
- <sup>30</sup>O. C. Zienkiewicz and R. L. Taylor, *The Finite Element Method*, 5th ed. (Butterworth-Heinemann, Boston, MA, 2000).
- <sup>31</sup>M. S. Bazaraa, H. D. Sherali, and C. M. Shetty, *Nonlinear Programming: Theory and Algorithms*, 2nd ed. (Wiley, New York, NY, 1993).